Electrocatalytic and Selective Oxidation of Glycerol to Formate on 2D 3d-Metal Phosphate Nanosheets and Carbon-Negative Hydrogen Generation

Published as part of ACS Materials Au virtual special issue "Celebrating the 25th Anniversary of the Chemical Research Society of India".

Inderjeet Chauhan, Pothoppurathu M. Vijay, Ravi Ranjan, Kshirodra Kumar Patra, and Chinnakonda S. Gopinath*

Cite This: *ACS Mater. Au* 2024, 4, 500−511

Read Online

ACCESS | Metrics & More | Article Recommendations | SI Supporting Information

ABSTRACT: In the landscape of green hydrogen production, alkaline water electrolysis is a well-established, yet not-so-cost-effective, technique due to the high overpotential requirement for the oxygen evolution reaction (OER). A low-voltage approach is proposed to overcome not only the OER challenge by favorably oxidizing abundant feedstock molecules with an earth-abundant catalyst but also to reduce the energy input required for hydrogen production. This alternative process not only generates carbon-negative green H_2 but also yields concurrent value-added products (VAPs), thereby maximizing economic advantages and transforming waste into valuable resources. The essence of this study lies in a novel electrocatalyst material. In the present study, unique and two-dimensional (2D) ultrathin nanosheet phosphates featuring first-row transition metals are synthesized by a one-step solvothermal method, and evaluated for the electrocatalytic glycerol oxidation reaction (GLYOR) in an alkaline medium and simultaneous H_2 production. $Co_3(PO_4)_2$ (CoP), $Cu_3(PO_4)_2$ (CuP), and $Ni_3(PO_4)_2$ (NiP) exhibit 2D sheet morphologies, while $FePO_4$ (FeP) displays an entirely different snowflake-like morphology. The 2D nanosheet morphology provides a large surface area and a high density of active sites. As a GLYOR catalyst, CoP ultrathin (~5 nm) nanosheets exhibit remarkably low onset potential at 1.12 V (vs RHE), outperforming that of NiP, FeP, and CuP around 1.25 V (vs RHE). CoP displays 82% selective formate production, indicating a superior capacity for C−C cleavage and concurrent oxidation; this property could be utilized to valorize larger molecules. CoP also exhibits highly sustainable electrochemical stability for a continuous 200 h GLYOR operation, yielding 6.5 L of H_2 production with a 4 cm^2 electrode and 98 ± 0.5% Faradaic efficiency. The present study advances our understanding of efficient GLYOR catalysts and underscores the potential of sustainable and economically viable green hydrogen production methodologies.

KEYWORDS: *2D material, electrolysis, earth-abundant material, sustainable development goals, Green H_2*

1. INTRODUCTION

The imperative quest for clean and renewable energy sources, driven by the increasing challenges of environmental damage and energy crises, has spurred intense research on viable alternatives. Solar, wind, and green hydrogen energy have emerged as pivotal contenders, garnering widespread attention for their potential to mitigate the adverse impacts of conventional energy production methods.[1−3] Among these, molecular hydrogen stands out as an attractive and carbon-neutral clean energy carrier, offering promise for a sustainable future.[4,5] Presently, the predominant method for hydrogen production, steam methane reforming, is marred by its unsustainability, as it relies heavily on fossil fuels and has a large amount of CO_2 emission.[6] Electrocatalytic water splitting is a compelling solution due to its capability of generating high-purity hydrogen, except for its cost. Nonetheless, this method

is envisioned as a key player in the future hydrogen economy, providing an environmentally favorable alternative.[7−9] However, the current challenges in electrocatalytic water splitting are the high overpotentials required for the anodic oxygen evolution reaction (OER), leading to suboptimal energy conversion efficiency. Despite the theoretical voltage requirement of 1.23 V for OER, commercial electrolyzers typically operate at voltages around 2.0 V and higher.[10] Moreover, the coproduction of O_2 at the anode introduces the risk of

hazardous mixing with H_2 at the cathode, even in the presence of high-cost/sophisticated membranes due to crossover. Furthermore, the formation of reactive oxygen species in the presence of H_2, O_2, and catalysts poses a threat to the longevity of the electrolyzer, as it may degrade the membrane and reduce its operational lifespan.[11,12] These challenges underscore the need for innovative solutions that address the efficiency, safety, and longevity of electrocatalytic water splitting. Advancements in this field are crucial for realizing the full potential of hydrogen as a clean energy carrier and facilitating the transition toward a sustainable energy landscape.

The increasing global demand for sustainable energy resources has spurred intensive research into the development of efficient and environmentally benign catalysts for energy conversion processes. In this context, the selective electro-catalytic oxidation of glycerol is of particular significance due to its abundant availability as a byproduct in biodiesel production.[13] Glycerol, a trihydroxy sugar alcohol, presents a unique opportunity as a renewable feedstock for the synthesis of value-added products and as a potential energy carrier. It has been shown that various types of commercial products can be obtained by electrochemical conversion of glycerol oxidation, like glyceric acid, glycolic acid, lactic acid, and formic acid; indeed the industrial market value of formic acid (HCOOH) is the highest among these chemicals.[14] Methyl formate hydrolysis, which is one of the classic commercial processes for manufacturing formic acid, is often a difficult multistep process that operates at moderately high temperature (90−140 °C) and pressure (between 2 and 7 bar of methyl formate with steam) conditions.[15] Critically, the theoretical oxidation potential required to completely oxidize one molecule of glycerol into three molecules of formic acid is 0.69 V (vs RHE), which is much lower than the 1.23 V required for the OER under standard conditions.[16]

To date, the catalysts used for the glycerol oxidation reaction (GLYOR) have been primarily limited to noble metal-based catalysts, like Au,[17] AuPt,[18] Pt,[19] Pd,[20] PtSb,[21] and PtRuSn,[22] and non-noble metal-based catalysts, like NiOOH,[23−25] amorphous CoO_x,[26] $NiCo_2O_4/NF$,[27] Co-doped Ni−Fe,[28] $CuCo_2O_4$,[29] and $Ni_{0.33}Co_{0.67}(OH)_2@HOS/NF$.[30] However, the reaction pathways of GLYOR are intricate, resulting in the production of various C1−C3 intermediates due to the difficulties in efficient C−C bond cleavage. This complexity necessitates the development of nonprecious earth-abundant electrocatalysts for a highly efficient, low onset/overpotential, and selective GLYOR to possibly a single product. Therefore, it is crucial to explore alternatives to noble metals, considering their cost and availability constraints. The development of nonprecious metal catalysts could enhance the economic and environmental sustainability of the GLYOR process, addressing the challenges associated with the current noble metal-dominated catalyst landscape. Transition metal-based catalysts have emerged as promising candidates for catalyzing the GLYOR, offering a diverse range of active sites and redox capabilities. Among them, the synthesis of ultrathin two-dimensional (2D) nanosheets has garnered substantial attention for their intrinsic properties, including the high surface area, tunable composition, and enhanced catalytic activity.[31,32]

In this study, we present the synthesis of two-dimensional (2D) ultrathin nanosheet phosphates, specifically with Co, Cu, and Ni, and a three-dimensional (3D) snowflake-like structure with Fe. CoP serves as a high-performance electrocatalyst for the GLYOR in an alkaline electrolyte medium. The design rationale involves the use of a transition metal phosphate with a 2D nanosheet structure, with the aim of providing a large surface area and a high density of surface-exposed active sites. Among the phosphates, CoP demonstrates a low onset potential and superior intrinsic stability in an alkaline electrolyte. As a GLYOR catalyst, ultrathin CoP nanosheets with a thickness of ∼5 nm exhibit a remarkably lower onset at 1.12 V vs RHE than other phosphates. This value is significantly lower, and, to the best of our knowledge, this is the first phosphate-based study for glycerol oxidation. Furthermore, the optimal ultrathin CoP catalyst demonstrates highly durable electrochemical stability during 200 h of continuous GLYOR under alkaline conditions.

2. EXPERIMENTS AND CHARACTERIZATION

2.1. Materials and Chemical Reagents

Cobalt, copper, iron, and nickel phosphate catalysts were synthesized using a direct single-step solvothermal method. Cobalt chloride ($CoCl_2·6H_2O$), iron chloride ($FeCl_3$), nickel chloride ($NiCl_2·6H_2O$), copper chloride ($CuCl_2·2H_2O$), and monosodium phosphate (NaH_2PO_4) were used, as received (Merck). Glycerol ($C_3H_8O_3$), potassium hydroxide (KOH), hydrochloric acid (HCl), deuterium oxide (D_2O), potassium hydrogen phthalate (KHP), formic acid (HCOOH), glycolic acid ($C_2H_4O_3$), glyceric acid ($C_3H_6O_4$), lactic acid ($C_3H_6O_3$), acetic acid (CH_3COOH), acetone (C_3H_6O), ethanol (C_2H_5OH), and isopropyl alcohol (IPA) were purchased from TCI Chemicals. Commercial 20% Pt/C was purchased from the Merck Industry. All precursors and other chemicals were used as received. Ni foam (thickness: 0.5 mm; porosity: ∼98%) was purchased from Global Nanotech, Mumbai, and used after cleaning.

2.2. Material Characterization

The powder X-ray diffraction (XRD) patterns of the materials were evaluated to obtain the structure and phase purity using a Rigaku Miniflex-600 diffractometer with Cu Kα radiation (λ = 1.5418 Å). The morphology and compositional information of the phosphates were obtained using field-emission scanning electron microscopy (FESEM; Nova Nano SEM 450). High-resolution transmission electron microscopy (HRTEM), high-angle annular dark-field-scanning transmission electron microscopy (HAADF-STEM), and chemical mapping images were recorded using a JEOL JEM F-200 instrument operating at 200 kV. The TEM and HRTEM samples were prepared by depositing a very small amount of well-dispersed material in IPA on a carbon-coated 200 mesh copper grid and drying for 1 h. Atomic force microscopy (AFM) experiments were carried out using a CSI Nano-Observer instrument. The oxidation states of the constituent elements were determined using an X-ray photo-electron spectroscopy (XPS) (Thermo Scientific Kα) spectrometer operated with a monochromatic X-ray source (Al Kα anode: 1486.6 eV). Adventitious carbon appearing at 284.6 eV was used for any static charge correction. ^1H and ^{13}C NMR spectra were recorded on an AV-NEO 400 spectrometer, and a Bruker BioSpin AG system (400 MHz) was used to analyze and quantify the liquid products. The evolved gas was analyzed by gas chromatography (GC Agilent 7890A), equipped with a thermal conductivity detector (at 200 °C). Raman vibrational features were identified using a TechnoS IndiRAM CTR 500C Micro Raman Spectrometer with an excitation laser wavelength of 532 nm.

2.3. Electrochemical Measurements

2.3.1. Fabrication of the Working Electrode. The electrodes were prepared using a drop-casting technique, which involved cleaning of Ni foam (NF) with 1 M HCl ultrasonically for 30 min, followed by sequential rinsing in deionized water and ethanol, with each step lasting 10 min in a sonication bath. NF was then dried in a vacuum oven at 70 °C for 10 h. In a typical procedure, 3 mg of the M-PO_4 nanocatalyst was dispersed in a mixture of IPA and Milli-Q water
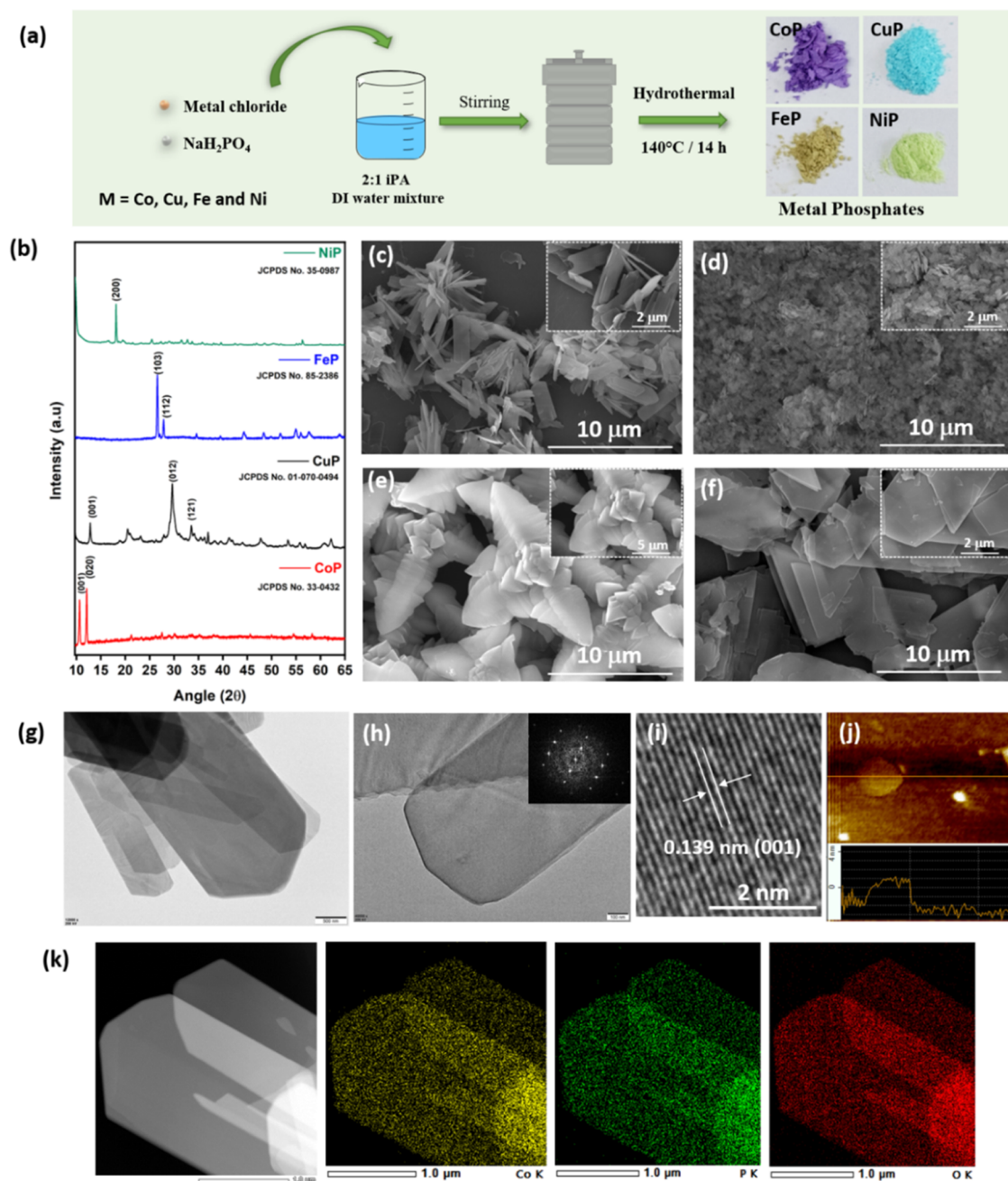
Figure 1. Synthesis and microscopy characterization of M-PO$_4$ (M = Co, Cu, Ni, and Fe) catalysts. (a) Schematic illustration of the M-PO$_4$ synthesis procedure. (b) XRD patterns of the as-prepared M-PO$_4$ samples. FESEM images of (c) CoP, (d) CuP, (e) FeP, and (f) NiP; insets in all these panels show FESEM images recorded at higher magnification. (g) TEM image of CoP, (h, i) HRTEM image of CoP, and SAED pattern (inset) obtained from (i) and (j) AFM images of single sheets of CoP to display the nanolevel (∼3−4 nm) thickness. (k) HAADF−STEM−EDS elemental maps of the CoP nanosheets for Co, P, and O, and their uniform distribution observed all over the nanosheet.

(3:1), drop-cast onto an NF substrate (1 × 1 cm^2), and vacuum-dried for 12 h. For stability testing in the electrolyzer, a CoP electrode was prepared using a spray-coating method with a catalyst loading of 3 ± 0.1 mg/cm^2.

Electrochemical experiments for the GLYOR, OER, and hydrogen evolution reaction (HER) were conducted using a Gamry reference 3000 potentiostat in the three- and two-electrode systems. The fabricated NF electrode served as the working electrode, while a graphite rod (5 mm diameter) and Pt/C on NF were used as counter electrodes for the HER in three-electrode and two-electrode systems, respectively. A saturated calomel electrode (SCE) was used as the reference electrode. All potentials are reported versus the reversible hydrogen electrode (RHE) according to the following equation

$$E_{RHE} = E_{SCE} + 0.05916 pH + 0.241 V \tag{1}$$

Polarization curves were obtained with 85% iR compensation, and all linear sweep voltammetry (LSV) curves were recorded at a sweep rate of 5 mV/s. The apparent current density was calculated based on the geometric area of the electrodes. The double-layer capacitance (C_{dl}) was determined from cyclic voltammetry (CV) curves recorded within a potential range, where no Faradaic current was observed. Various scan rates (10, 20, 40, 60, and 80 mV/s) were utilized, and plotting the cathodic charging currents against these rates allowed the determination of the C_{dl} slope. The ECSA was determined using the following equation.[33]

$$ECSA = C_{dl} / C_{NF} \tag{2}$$

The C_{dl} value, representing the double-layer capacitance of the NF substrate in 1.0 M KOH,[34] is denoted C_{NF}. According to the formula, there is a direct correlation between the ECSA and C_{dl}. In simpler terms, when C_{dl} increases, ECSA also increases.[35]

The liquid and gaseous products were analyzed and quantified using ^{1}H and ^{13}C NMR spectroscopy, and gas chromatography (GC). Chronopotentiometry tests in a three-electrode system at 10 mA/cm^2 were conducted for 15 h (0.1 M glycerol and 1 M KOH). Chronopotentiometry tests in a two-electrode system were carried out at 20 mA/cm^2 for 200 h to identify the glycerol oxidation products and to determine the respective Faradaic efficiencies for hydrogen production. For this purpose, 450 μL of the electrolyte was mixed with 130 μL of D$_2$O and 20 μL of KHP (as an internal standard). KHP was employed as an internal standard for the quantification of all products observed by ^{1}H NMR. The concentration of liquid products formed after the electrocatalytic reaction was calculated using the following formula

$$\frac{n_x}{n_y} = \frac{I_x}{I_y} \times \frac{N_y}{N_x} \tag{3}$$

Here, n_x represents the molar concentration of KHP, I_x represents the integral area in the ^{1}H NMR spectra for KHP, and N_x is the number of nuclei (4 equiv protons for KHP appearing at 7.25 ppm). Similarly, n_y is calculated from the above formula for the liquid product, I_y is the integral area of the product formed, and N_y is the number of nuclei associated with the peak. The concentration of the products obtained from the ^{1}H NMR spectroscopy was used to calculate the conversion, selectivity, and carbon balance.

$$\text{conversion (\%)} = \frac{n_{glycerol,initial} - n_{glycerol,final}}{n_{glycerol,initial}} \times 100 \tag{4}$$

$$\text{carbon balance (\%)} = \frac{n_{sum\ of\ products}}{3 \times n_{glycerol,initial}} \times 100 \tag{5}$$

$$\text{selectivity (\%)} = \frac{n_{product} \times \text{carbon balance}}{n_{sum\ of\ products}} \times 100 \tag{6}$$

where n is the number of moles.

2.3.2. Electrolyzer Setup. A flow electrolyzer with a geometrical area of 4 cm^2 was used in a two-electrode system, and a sustainion membrane was used to exchange the anion and separate the anode and cathode compartments for the GLYOR and HER. The flow plates were made of graphite. A constant current of 20 mA/cm^2 was used with a 3 mL/min flow rate of the solution (0.1 M glycerol + 1 M KOH) for longer stability with a peristatic pump.

$$\text{Faradaic efficiency (\%)} = \frac{n_{experimental}}{n_{theoretical}} \times 100 \tag{7}$$

where $n_{experimental}$ is the number of moles of H$_2$ collected experimentally. The theoretical amount of H$_2$ was calculated by the following equation

$$n_{theoretical} = \frac{Q}{n \times F} \tag{8}$$

where Q is the transferred charge, n is the number of electrons transferred to form one H$_2$ molecule, and F is the Faraday's constant (96,485 C/mol). The electricity consumption per m^3 of H$_2$ produced (W, kW per m^3 of H$_2$) is calculated as follows

$$W = \frac{n \times F \times V \times 1000}{3600 \times V_m} \tag{9}$$

where n represents the number of electrons transferred to produce each H$_2$ molecule, V denotes the applied voltage, and V_m is the molar volume of gas under standard temperature and pressure conditions (22.4 L/mol).

3. RESULTS AND DISCUSSION

In this study, metal (M = Co, Cu, Fe, and Ni) chloride precursors and monosodium phosphate were utilized for the synthesis of the corresponding metal phosphates using a single-step solvothermal process, as shown in Figure 1a. The synthesis process involved dissolving a 10 mM metal chloride and 20 mM phosphate precursor NaH$_2$PO$_4$ in a solvent mixture of isopropyl alcohol and ultrapure deionized water in a 2:1 ratio. This mixture resulted in a homogeneous solution, which was subsequently transferred into a 50 mL Teflon-lined stainless steel autoclave. The autoclave was then subjected to solvothermal treatment and maintained at 140 °C for 14 h in a hot air oven. Upon completion of the reaction, the autoclave was removed from the oven and allowed to cool naturally to the ambient temperature. Following the reaction, the products were filtered, subjected to multiple washes with deionized water, and finally washed with ethanol. The collected samples were then dried for 12 h in a vacuum oven, and then it was used to prepare the electrode for GLYOR. The color of the as-synthesized catalysts is shown in Figure 1a, and the catalysts are designated as CoP (violet), CuP (cyan), FeP (brown), and NiP (lime). The phase purity and crystallographic structures of the CoP, CuP, FeP, and NiP catalysts were determined using XRD. It should be noted that the environmentally benign hydrothermal synthesis of phosphate nanosheets is easy to scale up.

The narrow XRD patterns presented in Figure 1b demonstrate that the as-prepared metal phosphates exhibit a crystalline structure. CoP shows the formation of Co$_3$(PO$_4$)$_2$·8H$_2$O (JCPDS No.33-0432) with two major diffraction peaks at 10.57 and 12.09°, corresponding to the (001) and (020) crystallographic facets, respectively.[36] However, CuP (JCPDS No. 01-070-0494) displays major diffraction peaks at 12.71, 29.64, and 33.44°, which can be indexed to the (001), (012), and (121) facets, respectively.[37] FeP (JCPDS No. 85-2386) shows two major diffraction peaks at 26.62 and 27.8°, which can be indexed to (103) and (112) facets, respectively. NiP shows a major diffraction peak at 18.14° indexed to the (200) facet.[38] The layered 2D structure is evident from the XRD pattern, especially with high intensity for (00z) or (x00) with narrow features for all phosphates, except FeP. While NiP displays the (200) facet at 18.14°, CoP shows the (001) facet at 10.57°. The nanosheet morphology diminished in intensity for CuP, and a low-intensity (001) feature was observed. In contrast, FePO$_4$ does not display specific features for 2D morphology, which is supported by FESEM images (Figure 1e).

Morphological and microstructural analyses were conducted by using FESEM and HRTEM, respectively. A cursory look at the FESEM images reveals the influence of the cations on the morphology of the metal phosphates. Figure 1c,f shows bundles of sheet-like ultrathin 2D nanosheet structures for CoP and NiP, respectively; ultrathin nanosheets provide an almost transparent (for electron) appearance. The CoP appears to have a cactus−ovoid morphology with thin layers of CoP protruding from the center of the cacti. The square nanosheet and random morphology of CuP, depicted in Figure 1d, exhibit mixed morphological features. Nevertheless, a distinct morphological transformation is evident for FeP, as shown in Figure 1e, where a 3D snowflake morphology is observed. Figure 1g presents a TEM image providing detailed insight into the rectangular nanosheet structure of the CoP.
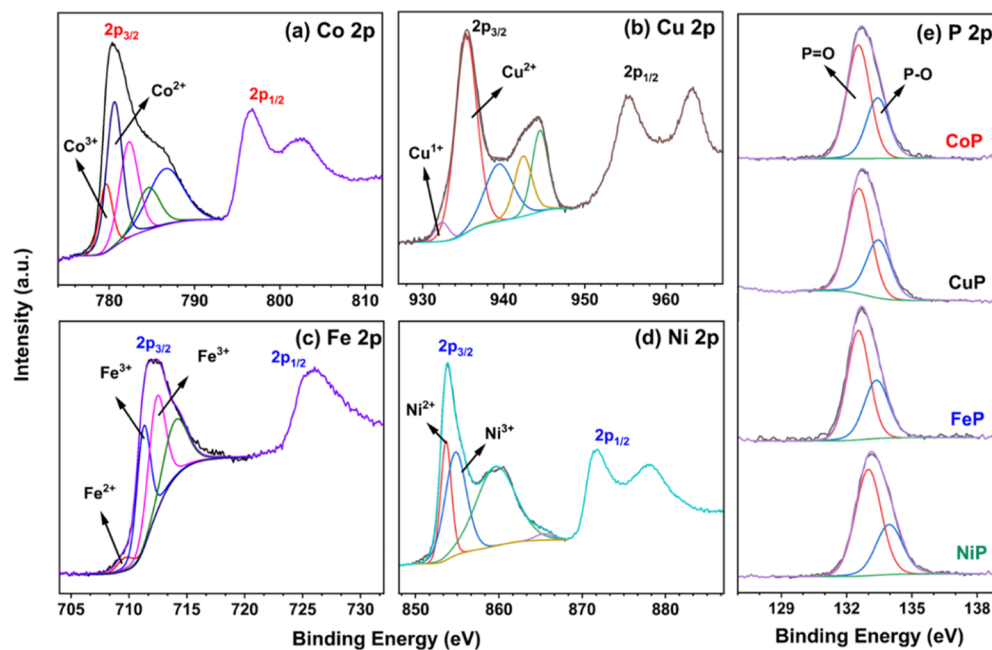
Figure 2. High-resolution XPS of (a) Co 2p, (b) Cu 2p, (c) Fe 2p, (d) Ni 2p, and (e) P 2p of the as-prepared metal phosphates.
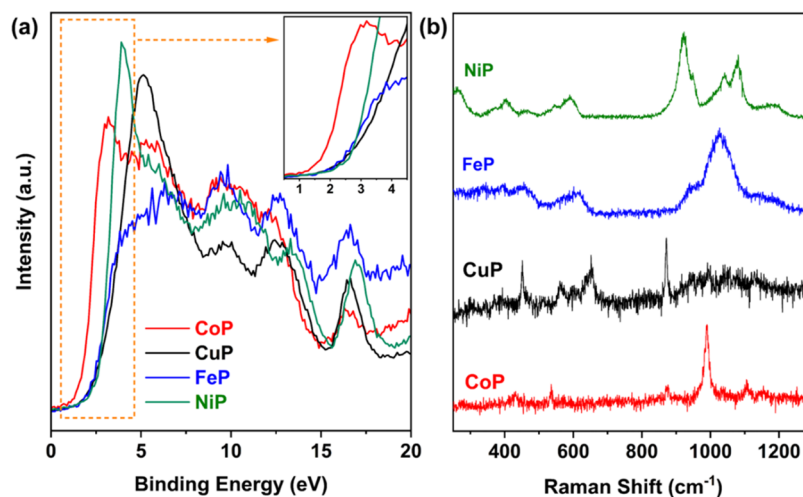

Figure 3. (a) X-ray valence band spectra of metal phosphates; the inset shows an enlarged view of VB onset. (b) Raman spectra of all metal phosphates.

Figure 1h,i shows the HRTEM images of the CoP. In Figure 1i, distinct lattice fringes are observed, revealing an interplanar spacing of 0.139 nm, which is attributed to the (001) facet of CoP, and matches the XRD data.[39] The selected area electron diffraction (SAED) pattern (inset) is shown in Figure 1i. To obtain more compositional information and understand the distribution of the constituent elements, additional investigations were conducted. Figure 1j shows the thickness of a single nanosheet of CoP, which is measured to be 3−4 nm; observation of such a thin nanosheet indicates the stacking of very few unit cells. Considering the unit-cell parameters of CoP ($a = b = 12.63$ Å, and $c = 5.017$ Å), 3−4-unit cells of CoP could be stacked into a single sheet. The hexagonal structure is evident from the nanosheet shown in TEM images (Figure 1g,h) and suggests a (001) facet. HAADF-STEM and elemental mapping in Figure 1k demonstrated the presence of cobalt (Co), phosphorus (P), and oxygen (O) as constituent elements in CoP. Moreover, a uniform distribution

of all elements throughout the nanosheets was observed. Analogous patterns of the HRTEM images and elemental mappings were observed for other phosphates, as shown in the Supporting Information (Figures S1−S3 for CuP, FeP, and NiP, respectively).

3.1. Electronic Structure of Metal Phosphates

The surface chemical characteristics of all metal phosphates were investigated by XPS. The survey spectrum (Figure S4) reveals the presence of four elements (Co, Cu, Fe, and Ni) on the surfaces of CoP, CuP, FeP, and NiP, respectively, apart from P and O. High-resolution XPS spectra of (a) Co 2p, (b) Cu 2p, (c) Fe 2p, and (d) Ni 2p core levels for CoP, CuP, FeP, and NiP, respectively, and (e) P 2p are displayed in Figure 2. Deconvolution was carried out using Casa XPS software, and a Shirley background removal procedure was applied to all spectra. The Co 2p core-level spectra (Figure 2a) exhibit a spin−orbit doublet along with prominent satellite features.
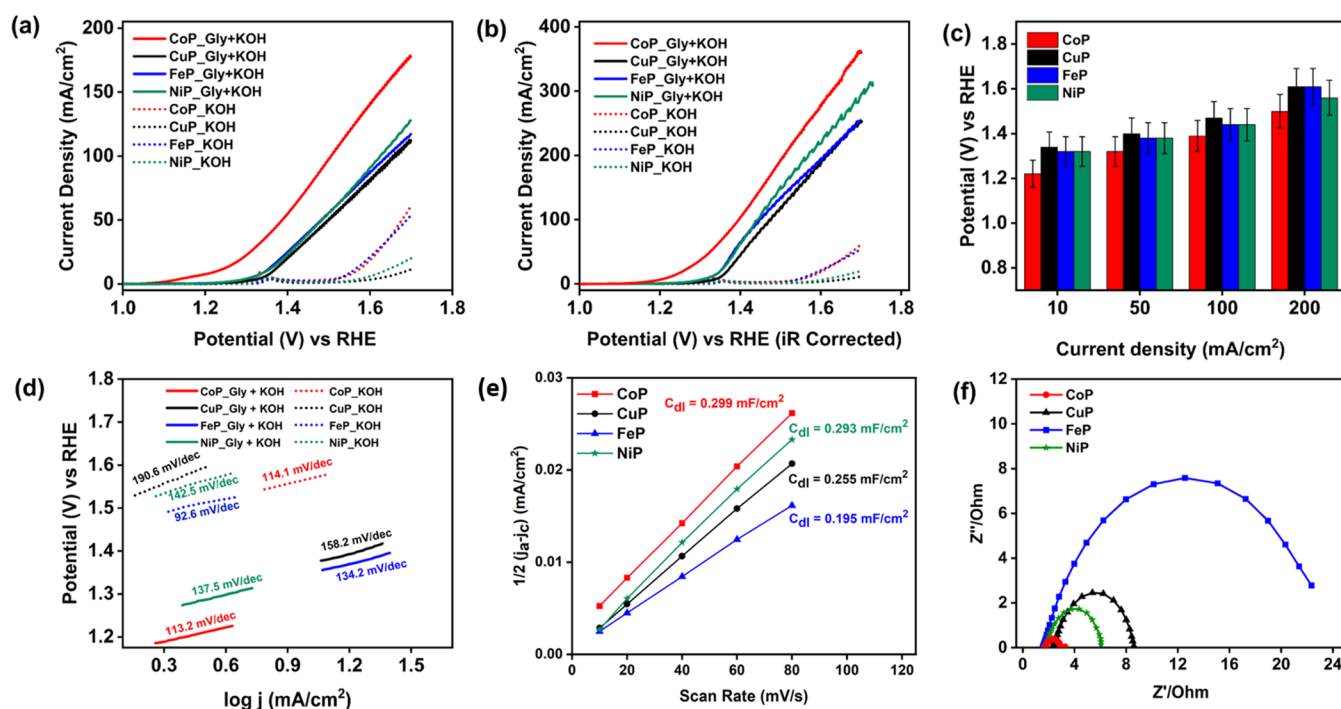
Figure 4. (a) Glycerol oxidation reaction (GLYOR) linear sweep voltammetry (LSV) curves (based on geometric current densities, mA/cm^2) for the series (Co, Cu, Fe, and Ni phosphate) on Ni foam at 5 mV/s in 0.1 M glycerol + 1 M KOH (solid line) with and without glycerol in 1 M KOH (dotted line). (b) 85% iR-corrected LSV curves. (c) Bar graph comparing the current densities for all phosphates. (d) Tafel plots of CoP, CuP, FeP, and NiP in 1 M KOH with and without 0.1 glycerol. (e) Capacitive current densities of different catalysts plotted against the scan rate of $10-80$ mV/s and corresponding double-layer capacitance (C_{dl}) values estimated through linear fitting of the plots. (f) Nyquist plots of different catalysts recorded at a given potential of 0.35 V (vs SCE) with a frequency range of $0.1-100$ kHz.

However, deconvolution indicates the presence of Co^{3+} ($2p_{3/2}$ at 779.6 eV) and Co^{2+} ($2p_{3/2}$ at 780.6 eV) oxidation states along with a subpeak at 782.3 eV and satellite features at a high binding energy (BE).[40] Similarly, a minor amount of Cu^{1+} ($2p_{3/2}$ at 932.2 ± 0.2 eV) and the majority of Cu^{2+} ($2p_{3/2}$ at 935.2 ± 0.2 eV) were observed with CuP (Figure 2b). The low-intensity feature observed at 932.2 eV is attributed to a possible reduction of Cu^{2+} to Cu^{1+} due to X-ray exposure.[41] The Fe $2p_{3/2}$ and $2p_{1/2}$ spin−orbit doublet exhibits multiple splitting and a very weak satellite, as depicted in Figure 2c for FeP. For FeP, Fe^{3+} (as in Fe_3O_4), Fe^{3+} (as in $Fe-PO_4$), and $Fe_3(PO_4)_2$ were observed at BEs of 711.2 ± 0.2, 712.4 ± 0.1 eV, and 714.2 ± 0.1 eV, respectively.[42] A minor peak observed at 709.6 ± 0.2 eV is attributed to the reduction of Fe^{3+} to Fe^{2+} due to X-ray exposure. In contrast, the XPS spectrum of Ni shows characteristic peaks for Ni^{2+} and Ni^{3+} at BEs of 853.5 ± 0.2 eV and 855.0 ± 0.2 eV, respectively, in Figure 2d, along with a broad satellite feature around 861 eV.[43]

Figure 2e shows the P 2p core-level spectra for all catalysts. The spectra show a broad peak, which upon deconvolution, reveals the $2p_{3/2}$ and $2p_{1/2}$ spin−orbit doublet centered at 133.0 and 133.9 eV, respectively, for all $M-PO_4$, except NiP. The O 1s for all phosphates recorded are shown in Figure S5; deconvolution shows three peaks at 530.5 ± 0.2, 531.5 ± 0.2, and 532.8 ± 0.2 eV. The first two features are attributed to O atoms predominantly associated with octahedral and tetrahedral coordination. The third feature at 532.8 eV is attributed to atmospheric contamination components, like water, CO_2.[44]

The X-ray valence band (XVB) spectra of all of the $M-PO_4$ catalysts are shown in Figure 3a. In the XVB spectra, the highest occupied VB appears between 1 and 5 eV for all catalysts. However, the presence of an intense main VB is

attributed to the contributions of the M (Co, Cu, Fe, and Ni) 3d and O 2p orbitals. Interestingly, the CoP shows a distinct onset of VB at the lowest BE, compared to all other phosphates. Compared to the VB onset of NiP, the same for CoP is shifted by 0.7 eV to the lower BE. In general, the VB feature appearing at low energy corresponds to higher activity, while high BE features indicate reduced activity or greater stability of the material. Co metal oxidation to various oxide states by in situ XPS reveals the presence of Co^{3+} 3d features at lower BE in the VB, followed by the Co^{2+} 3d feature.[45] This asserts the predominant contribution of Co 3d orbitals to the electronic structure, while CuP and FeP exhibit a combination of metal 3d orbitals along with the O 2p orbitals. The NiP exhibits intermediate characteristics between the two sets. Further, the VB onset of NiP, FeP, and CuP are at the same BE, and the VB maximum appears at the lowest BE for NiP, followed by CuP and FeP. This indicates a trend in activity from high to low (CoP-NiP-CuP $\sim$ FeP), which is in conformity with the LSV results shown later.

3.2. Raman Spectral Studies

Raman spectra were recorded for $M-PO_4$, mainly to understand the structural aspects, and the Raman results are shown in Figure 3b. Distinct peaks corresponding to the vibrational modes of the free oxo-anion $(PO_4)^{3-}$ were observed in metal phosphates, encompassing a singlet (A_1) at approximately 971 cm^{-1}, a doublet (E) at around 465 cm^{-1}, and two triply degenerate (F_2) modes, namely ν_3 at 1027 and ν_4 at 567 cm^{-1}. The symmetric and asymmetric stretching modes of the P−O bonds were associated with ν_1 and ν_3, while ν_2 and ν_4 primarily involved O−P−O symmetric and asymmetric bending modes, with a minor contribution from P vibration.[46] In CoP, the
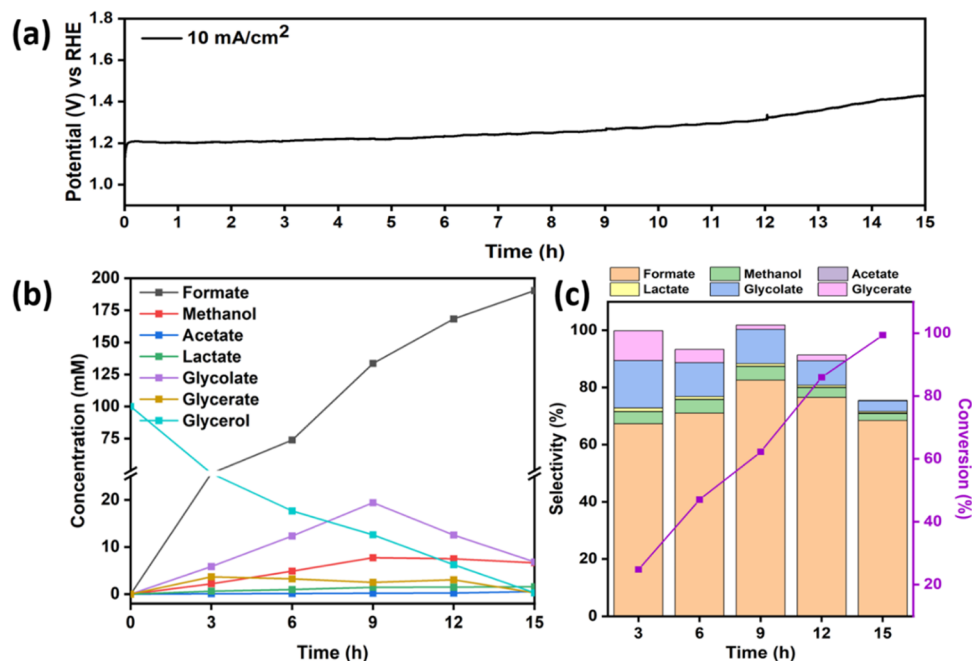
Figure 5. (a) Time-dependent chronopotentiometry (CP) reaction carried out at a constant current density of 10 mA/cm^2 for glycerol conversion using a CoP electrocatalyst. (b) Quantification of glycerol conversion and reaction products by ^{1}HNMR spectroscopy with CoP. (c) Glycerol conversion and product selectivity observed over a period of 15 h at a constant CP.

most prominent symmetric stretching peak was identified at 989 cm^{-1}, with corresponding antisymmetric and bending modes appearing weak at approximately 1100 and 420 cm^{-1}, respectively.[47] CuP exhibited only faint characteristic peaks related to the vibrations of $(PO_4)^{3-}$. FeP displayed a broad and intense symmetric stretching peak at 1025 cm^{-1}, indicating a nondistorted $(PO_4)^{3-}$ tetrahedral structure. Notably, FeP showed typical bulk characteristics in morphology and Raman spectra, whereas other phosphates demonstrated either shifts or low-intensity Raman features, suggesting their 2D nature.[48] On the other hand, NiP exhibited both features of antisymmetric modes between 1050 and 1100 cm^{-1}, with a red-shifted symmetric stretching peak at around 900 cm^{-1}. The split in the asymmetric stretching mode was attributed to the correlation effect induced by the coupling of Ni−O units in the structure.[46]

3.3. GLYOR Performance in an Alkaline Medium

Following a comprehensive analysis of the physical and chemical characteristics of the metal phosphates, electrochemical investigations of the GLYOR were conducted with electrocatalysts, as mentioned in Section 2. Given that the primary competing anodic reaction is the OER from water oxidation, an ideal GLYOR electrocatalyst should exhibit high activity toward glycerol oxidation and no (or limited) activity toward the OER. For comparison, water oxidation on these metal phosphate catalysts was also investigated under the same conditions in the absence of glycerol. The LSV polarization curves in Figure 4a depict the OER performance of metal phosphates, with and without 0.1 M glycerol. In the absence of glycerol, the metal phosphates demonstrated a notably high onset potential between the applied potential range of 1.55 to 1.68 V (vs RHE) required to achieve a current density of 10 mA/cm^2. In the presence of glycerol, the onset of GLYOR significantly decreased for all metal phosphates, indicating kinetically favorable glycerol oxidation over the OER.

Specifically, CoP exhibited the lowest onset potential at 1.12 V vs RHE, followed by NiP, FeP, and CuP at 1.24, 1.24, and 1.27 V vs RHE, respectively. The *iR*-corrected polarization curves in Figure 4b reaffirm the trend observed for the catalytic activity of the electrocatalysts toward GLYOR. It is crucial to note that the catalytic performance of metal phosphates is intrinsic to the catalysts themselves, as bare Ni foam exhibits poor catalytic activity for GLYOR. Figure 4c presents a comparison of the voltage required by all metal phosphate catalysts to achieve current densities of 10, 50, 100, and 200 mA/cm^2. The disparity in the potential for GLYOR is shown in Figure 4c. In Figure S6, at current densities of 10, 20, and 50 mA/cm^2, CoP exhibits potential differences of 340, 350, and 350 mV between the GLYOR and OER, respectively. Additionally, an assessment of the electrocatalytic kinetics for both GLYOR and OER was conducted by Tafel plot analysis derived from the LSV data, as shown in Figure 4d. This result highlights a considerably reduced Tafel slope value of 113.2 mV/dec, specifically for GLYOR with CoP nanosheets among the metal phosphates. These findings underscore the superior electrocatalytic GLYOR performance of CoPs compared to metal phosphates. It may be noted that the Tafel slopes for GLYOR and OER are comparable, except for CuP, but at different potentials.

The C_{dl} measurements (Figure 4e) show that the C_{dl} for CoP is 0.299 mF/cm^2. However, the capacitance values observed for NiP (0.293 mF/cm^2), CuP (0.255 mF/cm^2), and FeP (0.195 mF/cm^2) are almost similar to those of CoP. The C_{dl} values are calculated from the CV graphs at different scan rates, as shown in Figure S7. The measured C_{dl} values and the corresponding ECSA values of CoP (7.475 cm^2), NiP (7.325 cm^2), CuP (6.375 cm^2), and FeP (4.875 cm^2) indicate that all of the electrocatalysts have almost the same number of active sites.[49,50] However, the intrinsic activity of the CoP is significantly higher as compared to other metal phosphate catalysts, which resonates in the XPS-VB spectra (Figure 3a);
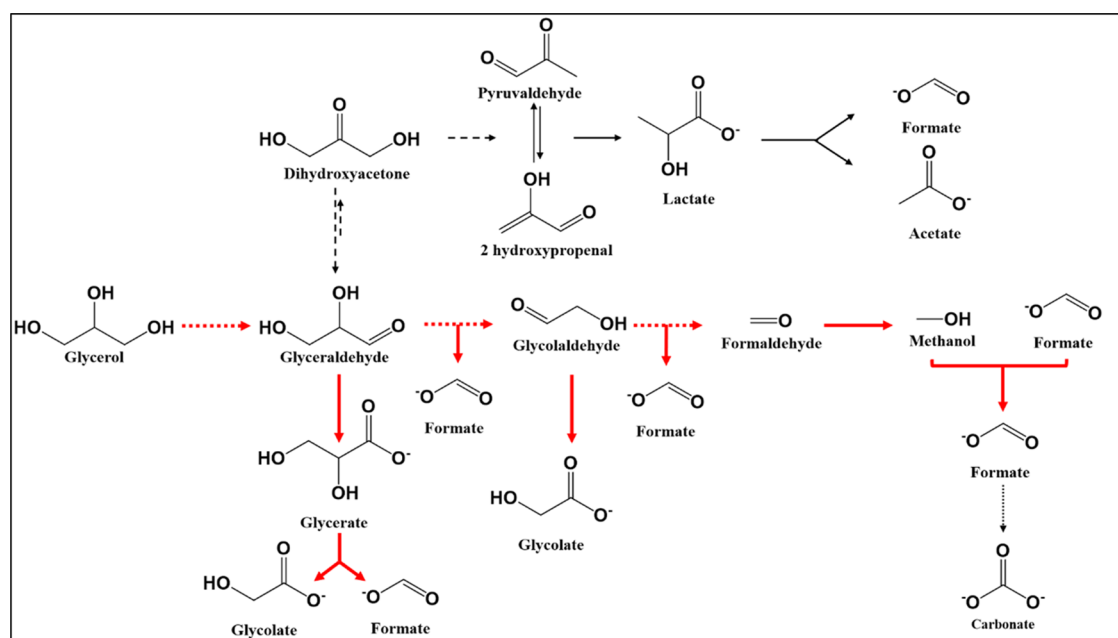
Figure 6. Proposed mechanistic pathway for the electrocatalytic oxidation of glycerol to formate on CoP in an alkaline medium, with emphasis on the suggested dominant pathways indicated by thick red arrows and dotted arrows showing unobserved intermediates. Solid and dashed black arrows indicate minor and alternate pathways for product formation.

CoP exhibits the lowest VB energy among phosphates, which leads to enhanced GLYOR activity.

To further investigate the interfacial reaction behavior of the catalyst, electrochemical impedance spectroscopy (EIS) was carried out. The EIS Nyquist plots presented in Figure 4f show a notable reduction in the charge transfer resistance (R_{ct}) of CoP compared to the other catalysts. Specifically, the R_{ct} of CoP (3 Ω) is significantly smaller than those of NiP (6.06 Ω), CuP (8.59 Ω), and FeP (24.62 Ω), indicating accelerated charge transfer kinetics between the CoP electrode and electrolyte. Despite the almost similar number of active sites in all electrocatalysts, CoP exhibited accelerated charge transfer behavior, which was mainly due to the high intrinsic activity of the active sites present, which enhanced GLYOR activity.

To assess the long-term performance of GLYOR and its anodic products, constant chronopotentiometry (CP) was conducted at 10 mA/cm² for 15 h. The stability of CoP was observed for the initial 12 h of CP, after which formate oxidation commenced (to carbonate) due to a decrease in the glycerol concentration and an increase in the OER. Consequently, achieving and maintaining a current density of 10 mA/cm² required an increase in the potential (Figure 5a). A significant potential increase during glycerol oxidation after about 12 h suggests the onset of formate oxidation to carbonate. Furthermore, the reaction mechanism was investigated by quantifying the 3 h interval samples using ¹H NMR analysis, as depicted in Figure 5b. A detailed carbon balance study was also conducted after each 3 h duration of the GLYOR process, and the results are listed in Table S1 in the Supporting Information. A decrease in glycerol content and a concurrent increase in formate concentration, as a function of reaction time along with near 100% carbon balance in 9 h suggest a 100% efficient conversion of glycerol to formate in 15 h (Figure 5b). The major intermediates detected in GLYOR included glycerate, glycolate, and methanol, while acetate and lactate were minor intermediates, as shown by ¹H NMR spectroscopy (Figure S8). As shown in Figure 5c, at 9 h, the

formate selectivity reaches 82%, and glycerol conversion is at ∼62%. Over time, formate undergoes further oxidation to carbonate due to the decreasing reactant availability, leading to a conversion exceeding 80% and formate selectivity reaching 78% at 12 h. By the end of 15 h, 100% glycerol conversion was achieved, although the carbon balance is less than 100% due to the significant formation of carbonate through continued oxidation of formate, which is evident from the small carbonate peak observed in the ¹³C NMR data (Figure S9). A similar kinetic study was conducted for CuP, FeP, and NiP, with quantification, and the glycerol conversion and product selectivity results are provided in Supporting Information (Figures S10−12 and Table S1). With NiP, under comparable conditions at a current density of 10 mA/cm², a noteworthy 93% glycerol conversion and 64% formate selectivity were observed after 12 h. However, the carbon balance diminished beyond this duration due to the continued oxidation of formate (Figure S12). Conversely, CuP and FeP exhibited lower conversion rates with approximately 50% selectivity for formate observed at a constant current density of 10 mA/cm² after 15 h. Notably, CuP and FeP necessitated an increase in the potential to achieve a desired current density of 10 mA/cm², leading to the oxidation of formate to CO₂ (Figure S13).

3.4. Proposed Mechanism Pathway for Glycerol Oxidation

The typical glycerol oxidation mechanism of a metal oxide or noble metal in an alkaline medium reported in the literature is as follows. First, a glycerol molecule is adsorbed on the catalyst surface, initiating dehydrogenation. This process leads to the formation of glycolaldehyde (GALD) or dihydroxyacetone (DHA), with subsequent reversible interconversion facilitated by base catalysis. Through a dehydration step, DHA can be transformed into pyruvaldehyde or 2-hydroxypropenal. These intermediates may undergo conversion into lactate via the Cannizzaro rearrangement, and subsequently, acetate and formate are produced through C−C cleavage (Figure 6).[51,52]
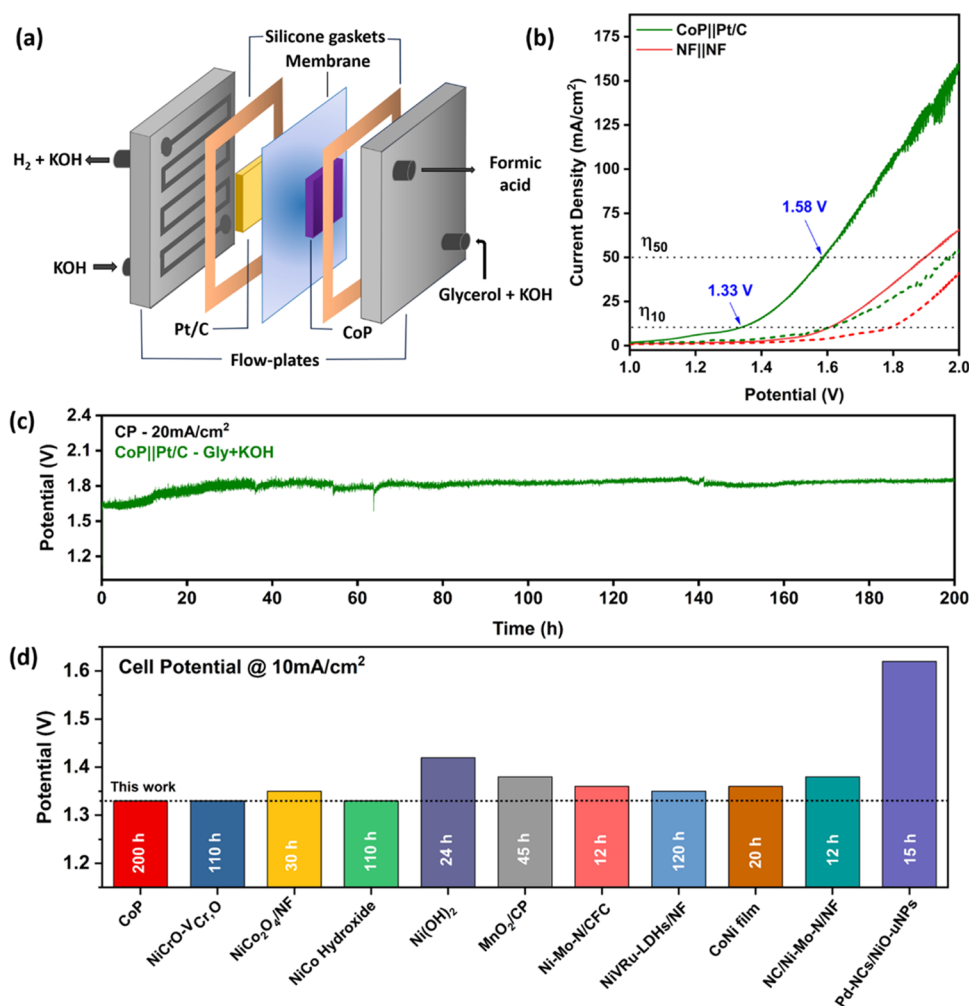
Figure 7. (a) Schematic of a two-electrode alkaline electrolyzer engaged in the GLYOR to formate at the anode and the HER at the cathode. (b) LSV plot observed for GLYOR in the electrolyzer, utilizing CoP/NF as the anode and Pt/C as the cathode (solid line, glycerol + KOH; dashed line, KOH). The same measurement was made on the NF also to rule out the GLYOR contribution. (c) Sustainability investigation of GLYOR at 20 mA/cm² was conducted using a two-electrode electrolyzer employing CoP∥Pt/C. (d) Comparison of the electrolytic efficiency of GLYOR at 10 mA/cm² for CoP with alternate electrocatalysts reported in the literature.

In the current work, it is evident from Figure 5 that high formate selectivity with significant selectivity for glycolate and glycerate indicates that oxidation occurs at either end of the terminal carbon. Although no glyceraldehyde was observed in the present work, it is very likely to undergo fast oxidation to glycerate and subsequently to glycolate and formate. Minor amounts of lactate and acetate formed in the current reaction (Figure 5c) also indicate that a parallel mechanism, to a small extent, occurs through DHA and pyruvaldehyde. The major conclusion that could be derived is the efficient oxidative C−C cleavage of glycerol and all intermediates, such as glycerate and glycolate, followed by preferential/selective oxidation to formate, on the CoP catalyst under the current experimental conditions. It is also evident from Figure 5c that, irrespective of the nature of intermediates, all of them undergo oxidation to formate. This concept may be extended to larger molecules with suitable catalysts under relevant conditions and more effort in this direction is desired.

3.5. Sustainable Performance Study for the CoP Catalyst

In the realm of water electrolysis, a critical hurdle lies in the imperative reduction of the operational potential to curtail the input electricity consumption. The substantial overpotential inherent to the OER in water splitting renders it exceptionally challenging to achieve a noteworthy reduction in power consumption beyond a certain threshold. Nevertheless, this obstacle was effectively overcome by the synergistic coupling of GLYOR and HER in a two-electrode electrolyzer configuration, as shown in Figure 7a.

The electrolyzer architecture featured a Pt/C cathode and a CoP anode spatially segregated by an anion-exchange membrane, with specific details provided in Section 2. Figure 7b shows the LSV plot for GLYOR in an alkaline electrolyzer, which reveals the concurrent electrochemical generation of hydrogen and formate at room temperature. At higher temperatures, between 60 and 75 °C, a large enhancement in electrolyzer activity performance is expected; therefore, it is worth performing this experiment. With the electrolyzer setup at room temperature, a current density of 10 mA/cm² (50 mA/cm²) was achieved at a notably low cell potential of 1.33 V (1.58 V), as shown in Figure 7b. Under these operational conditions, the system exhibited a simultaneous HER and glycerol oxidation performance. In contrast, a conventional water electrolysis experiment, employing a two-electrode setup with the same CoP∥Pt/C cell but devoid of glycerol

supplementation required a higher cell potential of 1.60 V (1.89 V) to attain an identical current density of 10 (50) mA/cm². Due to the significantly more advantageous thermodynamics of GLYOR on the CoP surface, the constructed electrolyzer necessitates just ~4.2 kWh/m³ of H_2 at a current density of 100 mA/cm². This is in stark contrast to the ~5.5 kWh/m³ of H_2 required by conventional alkaline electrolyzers. The remarkable low cell voltage exhibited by the CoP‖Pt/C system in the context of biomass component-assisted water splitting distinguishes it as an attractive feature relative to the majority of reported systems, as outlined in Table S2. Importantly, it is noteworthy that hydrogen constituted the exclusive gaseous product observed, with no oxygen- or carbon-containing byproducts, such as CO and CO_2. In addition, the sustainable performance of biomass component-based electrolysis was demonstrated via a chronoamperometry experiment for 200 h conducted at a current density of 20 mA/cm², and the results are shown in Figure 7c. It shows that the voltage remains constant at ~1.63 V throughout the 10 h operation for glycerol oxidation, and further the ~200 mV potential has been increased for secondary molecule oxidation, which is constant throughout the reaction and shows the stability of the catalyst. During the ongoing reaction within a 25 h time frame, the GLYOR sample was subjected to analysis via ¹H NMR. The results confirmed an increase in formate concentration, as depicted in Figure S14, along with glycerol conversion. Subsequently, after 75 h, the formate concentration decreased, which was attributed to its further oxidation to carbonates. To enhance the prolonged efficacy of the catalyst, the electrolyte was introduced into the solution after 75 h. Under a constant current density (CP) of 20 mA/cm², the hydrogen production rate remained constant at an average of 32.5 mL/h throughout the continuous operation of the overall reaction. The Faradaic efficiency of the HER was determined to be approximately 98%. The calculation of the FE for the HER involved a thorough analysis comparing the theoretical and experimental H_2 production, and detailed calculations are provided in Section 2. The catalytic performance of CoP is either comparable to or better than that of other electrocatalysts documented in the literature for overall electrolysis with GLYOR under the same conditions (Figure 7d). However, the current study shows sustainability for longer hours, along with a very high selectivity for formate production. This is depicted in Figure 7d, and many other catalysts are listed in Table S2. FESEM characterization (Figure S15) carried out after 200 h GLYOR (Figure 7c) exhibits intact nanosheet morphology, except for some agglomeration. The XRD pattern remains the same, as that observed in Figure 1b. These results indicate that the CoP catalyst remains stable and does not undergo any changes due to the prolonged reaction.

4. CONCLUSIONS

In conclusion, this study elucidates a distinctive morphology-dependent selectivity for formate and glycerol conversion on metal phosphates, showing simultaneous and highly efficient electrocatalytic hydrogen generation. Cobalt phosphate (CoP) has been identified as a novel and proficient catalyst, demonstrating both efficiency and stability in the selective production of formate through glycerol oxidation under alkaline conditions at ambient temperature. Particularly, ultrathin 2D-CoP nanosheets exhibit very high selectivity, achieving 82% formate yield compared to other phosphates.

The electrochemical oxidative cleavage of the C−C bond is more favorable for CoP than for NiP, FeP, and CuP catalysts. The coupling of the anodic GLYOR and cathodic HER within the CoP‖Pt/C two-electrode electrolyzer yields a current density of 10 mA/cm² with a minimal cell voltage of 1.33 V. Continuous operation of the GLYOR for over 8 days (24 × 7) indicates the enduring stability of the CoP catalyst under the present experimental conditions. Utilizing the earth-abundant transition metal phosphate for the electrocatalytic oxidation of glycerol paves the way for innovative designs and exploration of economical ways of addressing the GLYOR. These catalysts offer efficient and selective electrochemical glycerol oxidation, yielding formate and other value-added chemicals along with the production of environmentally friendly hydrogen resources.

The engineered CoP catalyst exhibits remarkable efficiency in catalyzing the conversion of glycerol to formate, thereby demonstrating promising prospects for its application in the conversion of diverse biomass feedstocks, including glucose, starch, and cellulose. The selective C−C cleavage strategy presented in this study is worth exploring with any of the larger molecules listed above and may be evaluated for depolymerization of low-molecular-weight polymers. Furthermore, carrying out electrocatalytic conversions at significantly higher temperatures (50 and 75 °C) is expected to substantially improve the performance. Another important aspect is the production of hydrogen under such conditions, which prudently employs waste/abundant carbon-containing molecules to produce value-added products; hence, the generated hydrogen becomes carbon-negative green hydrogen. This type of route may prove to be helpful in achieving net-zero targets sooner. Nonetheless, more work is required in this direction.

■ ASSOCIATED CONTENT

ⓢ Supporting Information

The Supporting Information is available free of charge at https://pubs.acs.org/doi/10.1021/acsmaterialsau.4c00024.

> HRETM images of CuP, FeP, and NiP (Figures S1−S3); XPS survey spectra of all M-PO₄ (Figure S4), O 1s XPS spectra (Figure S5); potential differences between GLYOR and OER in the CoP nanosheet (Figure S6); double-layer capacitance (C_{dl}) calculation (Figure S7); ¹H NMR spectra of the intermediate products (Figure S8); ¹³C NMR spectra of GLYOR (Figure S9); GLYOR reaction, and selectivity conversion graph of CuP, FeP, and NiP (Figures S10−S12); chronopotentiometry reaction graph of all M-PO₄ (Figure S13); ¹H NMR spectra of GLYOR in an electrolyzer system with CoP‖Pt/C (Figure S14); FESEM images (Figure S15); selectivity, conversion, and carbon balance of all M-PO₄ (Table S1); and comparison table of recently reported work in GLYOR and other low oxidizing molecules (Table S2) (PDF)

■ AUTHOR INFORMATION

Corresponding Author

Chinnakonda S. Gopinath − *Catalysis and Inorganic Chemistry Division, CSIR-National Chemical Laboratory, Pune 411 008, India; Academy of Scientific and Innovative Research (AcSIR), Ghaziabad 201 002, India;* ⓞ orcid.org/0000-0002-4525-3912; Email: cs.gopinath@ncl.res.in

Authors

Inderjeet Chauhan − *Catalysis and Inorganic Chemistry Division, CSIR-National Chemical Laboratory, Pune 411 008, India; Academy of Scientific and Innovative Research (AcSIR), Ghaziabad 201 002, India*

Pothoppurathu M. Vijay − *Catalysis and Inorganic Chemistry Division, CSIR-National Chemical Laboratory, Pune 411 008, India*

Ravi Ranjan − *Catalysis and Inorganic Chemistry Division, CSIR-National Chemical Laboratory, Pune 411 008, India; Academy of Scientific and Innovative Research (AcSIR), Ghaziabad 201 002, India*

Kshirodra Kumar Patra − *Catalysis and Inorganic Chemistry Division, CSIR-National Chemical Laboratory, Pune 411 008, India;* orcid.org/0000-0002-1468-0946

Complete contact information is available at:
https://pubs.acs.org/10.1021/acsmaterialsau.4c00024

Author Contributions

CRediT: **Inderjeet Chauhan** conceptualization, investigation, writing-original draft, writing-review & editing.

Notes

The authors declare no competing financial interest.

■ REFERENCES

(1) Dresselhaus, M. S.; Thomas, I. L. Alternative Energy Technologies. *Nature* **2001**, *414* (6861), 332−337.

(2) Zhang, J.; Wang, H.; Tian, Y.; Yan, Y.; Xue, Q.; He, T.; Liu, H.; Wang, C.; Chen, Y.; Xia, B. Y. Anodic Hydrazine Oxidation Assists Energy-Efficient Hydrogen Evolution over a Bifunctional Cobalt Per selenide Nanosheet Electrode. *Angew. Chem., Int. Ed.* **2018**, *57* (26), 7649−7653.

(3) Gopinath, C. S.; Nalajala, N. A Scalable and Thin Film Approach for Solar Hydrogen Generation: A Review on Enhanced Photocatalytic Water Splitting. *J. Mater. Chem. A* **2021**, *9* (3), 1353−1371.

(4) Zhang, J.; Wang, T.; Liu, P.; Liao, Z.; Liu, S.; Zhuang, X.; Chen, M.; Zschech, E.; Feng, X. Efficient Hydrogen Production on MoNi$_4$ Electrocatalysts with Fast Water Dissociation Kinetics. *Nat. Commun.* **2017**, *8* (1), No. 15437.

(5) Rajaambal, S.; Sivaranjani, K.; Gopinath, C. S. Recent Developments in Solar H$_2$ Generation from Water Splitting. *J. Chem. Sci.* **2015**, *127* (1), 33−47.

(6) Navarro, R. M.; Peña, M. A.; Fierro, J. L. G. Hydrogen Production Reactions from Carbon Feedstocks: Fossil Fuels and Biomass. *Chem. Rev.* **2007**, *107* (10), 3952−3991.

(7) Holladay, J. D.; Hu, J.; King, D. L.; Wang, Y. An Overview of Hydrogen Production Technologies. *Catal. Today* **2009**, *139*, 244−260.

(8) Li, X.; Hao, X.; Abudula, A.; Guan, G. Nanostructured Catalysts for Electrochemical Water Splitting: Current State and Prospects. *J. Mater. Chem. A* **2016**, *4* (31), 11973−12000.

(9) Zheng, D.; Li, J.; Ci, S.; Cai, P.; Ding, Y.; Zhang, M.; Wen, Z. Three-Birds-with-One-Stone Electrolysis for Energy-Efficiency Production of Gluconate and Hydrogen. *Appl. Catal., B* **2020**, *277*, No. 119178.

(10) Qin, D.-D.; Tang, Y.; Ma, G.; Qin, L.; Tao, C.-L.; Zhang, X.; Tang, Z. Molecular Metal Nanoclusters for ORR, HER and OER: Achievements, Opportunities and Challenges. *Int. J. Hydrogen Energy* **2021**, *46* (51), 25771−25781.

(11) Rausch, B.; Symes, M. D.; Chisholm, G.; Cronin, L. Decoupled Catalytic Hydrogen Evolution from a Molecular Metal Oxide Redox Mediator in Water Splitting. *Science* **2014**, *345* (6202), 1326−1330.

(12) Wei, X.; Wang, S.; Hua, Z.; Chen, L.; Shi, J. Metal−Organic Framework Nanosheet Electrocatalysts for Efficient H$_2$ Production from Methanol Solution: Methanol-Assisted Water Splitting or Methanol Reforming? *ACS Appl. Mater. Interfaces* **2018**, *10* (30), 25422−25428.

(13) Kim, D.; Oh, L. S.; Tan, Y. C.; Song, H.; Kim, H. J.; Oh, J. Enhancing Glycerol Conversion and Selectivity toward Glycolic Acid via Precise Nanostructuring of Electrocatalysts. *ACS Catal.* **2021**, *11* (24), 14926−14931.

(14) Quispe, C. A. G.; Coronado, C. J. R.; Carvalho, J. A., Jr. Glycerol: Production, Consumption, Prices, Characterization and New Trends in Combustion. *Renewable Sustainable Energy Rev.* **2013**, *27*, 475−493.

(15) Bulushev, D. A.; Ross, J. R. H. Towards Sustainable Production of Formic Acid. *ChemSusChem* **2018**, *11* (5), 821−836.

(16) Rizk, M. R.; Abd El-Moghny, M. G. Controlled Galvanic Decoration Boosting Catalysis: Enhanced Glycerol Electro-Oxidation at Cu/Ni Modified Macroporous Films. *Int. J. Hydrogen Energy* **2021**, *46* (1), 645−655.

(17) Xie, Y.; Sun, L.; Pan, X.; Zhou, Z.; Zheng, Y.; Yang, X.; Zhao, G. Carbon Paper Supported Gold Nanoflowers for Tunable Glycerol Electrooxidation Boosting Efficient Hydrogen Evolution. *Carbon* **2023**, *203*, 88−96.

(18) Dai, C.; Sun, L.; Liao, H.; Khezri, B.; Webster, R. D.; Fisher, A. C.; Xu, Z. J. Electrochemical Production of Lactic Acid from Glycerol Oxidation Catalyzed by AuPt Nanoparticles. *J. Catal.* **2017**, *356*, 14−21.

(19) Zhang, Z.; Xin, L.; Li, W. Electrocatalytic Oxidation of Glycerol on Pt/C in Anion-Exchange Membrane Fuel Cell: Cogeneration of Electricity and Valuable Chemicals. *Appl. Catal., B* **2012**, *119−120*, 40−48.

(20) Chauhan, I.; Bajpai, H.; Ray, B.; Kolekar, S. K.; Datar, S.; Patra, K. K.; Gopinath, C. S. Electrocatalytic Glycerol Conversion: A Low Voltage Pathway to Efficient Carbon-Negative Green Hydrogen and Value Added Chemicals Production. *ACS Appl. Mater. Interfaces* **2024**, *16*, 26130−26141, DOI: 10.1021/acsami.4c02392.

(21) Lee, S.; Kim, H. J.; Lim, E. J.; Kim, Y.; Noh, Y.; Huber, G. W.; Kim, W. B. Highly Selective Transformation of Glycerol to Dihydroxyacetone without Using Oxidants by a PtSb/C-Catalyzed Electrooxidation Process. *Green Chem.* **2016**, *18* (9), 2877−2887.

(22) Kim, H. J.; Choi, S. M.; Green, S.; Tompsett, G. A.; Lee, S. H.; Huber, G. W.; Kim, W. B. Highly Active and Stable PtRuSn/C Catalyst for Electrooxidations of Ethylene Glycol and Glycerol. *Appl. Catal., B* **2011**, *101* (3−4), 366−375.

(23) Choi, S.; Balamurugan, M.; Lee, K.-G.; Cho, K. H.; Park, S.; Seo, H.; Nam, K. T. Mechanistic Investigation of Biomass Oxidation Using Nickel Oxide Nanoparticles in a CO$_2$-Saturated Electrolyte for Paired Electrolysis. *J. Phys. Chem. Lett.* **2020**, *11* (8), 2941−2948.

(24) Taitt, B. J.; Nam, D.-H.; Choi, K.-S. A Comparative Study of Nickel, Cobalt, and Iron Oxyhydroxide Anodes for the Electrochemical Oxidation of 5-Hydroxymethylfurfural to 2,5-Furandicarboxylic Acid. *ACS Catal.* **2019**, *9* (1), 660−670.

(25) Li, J.; Wei, R.; Wang, X.; Zuo, Y.; Han, X.; Arbiol, J.; Llorca, J.; Yang, Y.; Cabot, A.; Cui, C. Selective Methanol-to-Formate Electrocatalytic Conversion on Branched Nickel Carbide. *Angew. Chem., Int. Ed.* **2020**, *59* (47), 20826−20830.

(26) Vo, T.-G.; Ho, P.-Y.; Chiang, C.-Y. Operando Mechanistic Studies of Selective Oxidation of Glycerol to Dihydroxyacetone over Amorphous Cobalt Oxide. *Appl. Catal., B* **2022**, *300*, No. 120723.

(27) Wu, G.; Dong, X.; Mao, J.; Li, G.; Zhu, C.; Li, S.; Chen, A.; Feng, G.; Song, Y.; Chen, W.; Wei, W. Anodic Glycerol Oxidation to Formate Facilitating Cathodic Hydrogen Evolution with Earth-Abundant Metal Oxide Catalysts. *Chem. Eng. J.* **2023**, *468*, No. 143640.

(28) Zhong, Z.; Li, M.; Wang, J.; Lin, J.; Pan, J.; Jiang, S.; Xie, A.; Luo, S. Co-Doped Ni−Fe Spinels for Electrocatalytic Oxidation over Glycerol. *Int. J. Hydrogen Energy* **2022**, *47* (29), 13933−13945.

(29) Han, X.; Sheng, H.; Yu, C.; Walker, T. W.; Huber, G. W.; Qiu, J.; Jin, S. Electrocatalytic Oxidation of Glycerol to Formic Acid by $CuCo_2O_4$ Spinel Oxide Nanostructure Catalysts. *ACS Catal.* **2020**, *10* (12), 6741−6752.

(30) Pei, Y.; Pi, Z.; Zhong, H.; Cheng, J.; Jin, F. Glycerol Oxidation-Assisted Electrochemical CO_2 Reduction for the Dual Production of Formate. *J. Mater. Chem. A* **2022**, *10* (3), 1309−1319.

(31) Wang, Y.; Zhang, M.; Liu, Y.; Zheng, Z.; Liu, B.; Chen, M.; Guan, G.; Yan, K. Recent Advances on Transition-Metal-Based Layered Double Hydroxides Nanosheets for Electrocatalytic Energy Conversion. *Adv. Sci.* **2023**, *10* (13), No. 2207519.

(32) Xie, H.; Li, Z.; Cheng, L.; Haidry, A. A.; Tao, J.; Xu, Y.; Xu, K.; Ou, J. Z. Recent Advances in the Fabrication of 2D Metal Oxides. *iScience* **2022**, *25* (1), No. 103598.

(33) Yang, J.; Xiao, Y.; Zhao, Q.; Zhang, G.; Wang, R.; Teng, G.; Chen, X.; Weng, M.; He, D.; Mu, S.; Lin, Y.; Pan, F. Synergistic Effect of Charge Transfer and Short H-Bonding on Nanocatalyst Surface for Efficient Oxygen Evolution Reaction. *Nano Energy* **2019**, *59*, 443−452.

(34) Li, N.; Ai, L.; Jiang, J.; Liu, S. Spinel-Type Oxygen-Incorporated Ni^{3+} Self-Doped Ni_3S_4 Ultrathin Nanosheets for Highly Efficient and Stable Oxygen Evolution Electrocatalysis. *J. Colloid Interface Sci.* **2020**, *564*, 418−427.

(35) Anantharaj, S.; Ede, S. R.; Sakthikumar, K.; Karthick, K.; Mishra, S.; Kundu, S. Recent Trends and Perspectives in Electrochemical Water Splitting with an Emphasis on Sulfide, Selenide, and Phosphide Catalysts of Fe, Co, and Ni: A Review. *ACS Catal.* **2016**, *6* (12), 8069−8097.

(36) Katkar, P. K.; Marje, S. J.; Kale, S. B.; Lokhande, A. C.; Lokhande, C. D.; Patil, U. M. Synthesis of Hydrous Cobalt Phosphate Electro-Catalysts by a Facile Hydrothermal Method for Enhanced Oxygen Evolution Reaction: Effect of Urea Variation. *CrystEngComm* **2019**, *21* (5), 884−893.

(37) Pujari, S. S.; Kadam, S. A.; Ma, Y.-R.; Jadhav, S. B.; Kumbhar, S. S.; Bhosale, S. B.; Gunjakar, J. L.; Lokhande, C. D.; Patil, U. M. Hydrothermally Synthesized Nickel Copper Phosphate Thin Film Cathodes for High-Performance Hybrid Supercapacitor Devices. *J. Energy Storage* **2022**, *52*, No. 105037.

(38) Sharma, P.; Radhakrishnan, S.; Khil, M.-S.; Kim, H.-Y.; Kim, B.-S. Simple Room Temperature Synthesis of Porous Nickel Phosphate Foams for Electrocatalytic Ethanol Oxidation. *J. Electroanal. Chem.* **2018**, *808*, 236−244.

(39) Bu, X.; Chiang, C.; Wei, R.; Li, Z.; Meng, Y.; Peng, C.; Lin, Y.; Li, Y.; Lin, Y.; Chan, K. S.; Ho, J. C. Two-Dimensional Cobalt Phosphate Hydroxide Nanosheets: A New Type of High-Performance Electrocatalysts with Intrinsic CoO_6 Lattice Distortion for Water Oxidation. *ACS Appl. Mater. Interfaces* **2019**, *11* (42), 38633−38640.

(40) Ranjan, R.; Tekawadia, J.; Jain, R.; Mhamane, N. B.; Raja, T.; Gopinath, C. S. Co_3O_4 for Sustainable CO_2 Reduction and Possible Fine-Tuning towards Selective CO Production. *Chem. Eng. J.* **2023**, *471*, No. 144459.

(41) Roy, K.; Gopinath, C. S. UV Photoelectron Spectroscopy at Near Ambient Pressures: Mapping Valence Band Electronic Structure Changes from Cu to CuO. *Anal. Chem.* **2014**, *86* (8), 3683−3687.

(42) Wang, Y.; Asunskis, D. J.; Sherwood, P. M. A. Iron (II) Phosphate $(Fe_3(PO_4)_2$ by XPS. *Surf. Sci. Spectra* **2002**, *9* (1), 91−98.

(43) Velu, S.; Suzuki, K.; Vijayaraj, M.; Barman, S.; Gopinath, C. S. In Situ XPS Investigations of $Cu_{1−x}Ni_xZnAl$-Mixed Metal Oxide Catalysts Used in the Oxidative Steam Reforming of Bio-Ethanol. *Appl. Catal., B* **2005**, *55* (4), 287−299.

(44) Jain, R.; Reddy, K. P.; Ghosalya, M. K.; Gopinath, C. S. Water Mediated Deactivation of Co_3O_4 Naonrods Catalyst for CO Oxidation and Resumption of Activity at and Above 373 K: Electronic Structural Aspects by NAPPES. *J. Phys. Chem. C* **2017**, *121* (37), 20296−20305.

(45) Reddy, K. P.; Jain, R.; Ghosalya, M. K.; Gopinath, C. S. Metallic Cobalt to Spinel Co_3O_4 —Electronic Structure Evolution by Near-Ambient Pressure Photoelectron Spectroscopy. *J. Phys. Chem. C* **2017**, *121* (39), 21472−21481.

(46) Ramana, C. V.; Ait-Salah, A.; Utsunomiya, S.; Becker, U.; Mauger, A.; Gendron, F.; Julien, C. M. Structural Characteristics of Lithium Nickel Phosphate Studied Using Analytical Electron Microscopy and Raman Spectroscopy. *Chem. Mater.* **2006**, *18* (16), 3788−3794.

(47) Mahmoud, B. A.; Mirghni, A. A.; Oyedotun, K. O.; Momodu, D.; Fasakin, O.; Manyala, N. Synthesis of Cobalt Phosphate-Graphene Foam Material via Co-Precipitation Approach for a Positive Electrode of an Asymmetric Supercapacitors Device. *J. Alloys Compd.* **2020**, *818*, No. 153332.

(48) Zhang, L.; Brow, R. K. A Raman Study of Iron−Phosphate Crystalline Compounds and Glasses. *J. Am. Ceram. Soc.* **2011**, *94* (9), 3123−3130.

(49) Jeon, S. S.; Kang, P. W.; Klingenhof, M.; Lee, H.; Dionigi, F.; Strasser, P. Active Surface Area and Intrinsic Catalytic Oxygen Evolution Reactivity of NiFe LDH at Reactive Electrode Potentials Using Capacitances. *ACS Catal.* **2023**, *13* (2), 1186−1196.

(50) Patra, K. K.; Gopinath, C. S. CO_2 Electrolysis towards Large Scale Operation: Rational Catalyst and Electrolyte Design for Efficient Flow-Cell. *Chem. Commun.* **2023**, *59* (45), 6774−6795.

(51) Terekhina, I.; White, J.; Cornell, A.; Johnsson, M. Electrocatalytic Oxidation of Glycerol to Value-Added Compounds on Pd Nanocrystals. *ACS Appl. Nano Mater.* **2023**, *6* (13), 11211−11220.

(52) Li, Y.; Wei, X.; Chen, L.; Shi, J.; He, M. Nickel-Molybdenum Nitride Nanoplate Electrocatalysts for Concurrent Electrolytic Hydrogen and Formate Productions. *Nat. Commun.* **2019**, *10* (1), No. 5335.